4. COLLECTIVE EFFECTS

INTRODUCTION

The proposed facility is designed to operate with a "flat bunch" requiring a small vertical emittance $\varepsilon_y \approx$ 0.4 mm-mrad, and large emittance ratio $\varepsilon_x/\varepsilon_y \approx 50$. Successful machine design depends critically upon emittance control from the election source at the rf photocathode to the radiation source point in undulators. The understanding and mitigation of collective effects is essential for emittance control. Key aspects of accelerator physics involved in beam break-up, coherent synchrotron radiation, resistive wall impedance and other effects have been examined and are reported here.

BEAM BREAK-UP

The Beam Break-Up (BBU) instability, generated by dipole modes in the linac excited by off-axis beam trajectories, can develop within a single bunch and lead to a dilution of the emittance [1]. As a bunch travels through an accelerating section, the head undergoes an unperturbed motion while the tail experiences a deflection due to the wakefield of preceding particles. Analogously, the same phenomenon can be observed when the structure is misaligned with respect to the ideal beamline, even if the bunch is injected on the nominal axis.

There are three aspects which require particular attention in the BBU analysis for a recirculating linac: the very wide energy range, 10 MeV to 2.5 GeV, (including the injector linac); the recirculation through the main linac, which requires taking into account the long-range as well as the short-range wake; and the absence of focussing elements in the linac, which precludes the use of usual analysis methods based on the assumption that the beam energy does not change significantly in a betatron wavelength.

The equation describing the transverse displacement *x(s,z)* of the electrons in an accelerated bunch, as a function of their longitudinal position within the bunch *z*, can be written in the form [2]:

$$\frac{d}{ds}\left[\gamma(s)\frac{dx}{ds}\right]+k^2(s)\gamma(s)x(s,z)=r_0\int_z^{\infty}\rho(z')W_{\perp}(z'-z)x(s,z')dz' \qquad (1)$$

where γ is the relativistic factor, k the focussing strength, r_0 the classical electron radius, ρ the bunch density, $W_{\perp}$ the transverse wake function per unit length and s indicates the position along the linac. We assume infinitesimally small transverse beam dimensions (a reasonable approximation, when the bunch dimensions are much less than the size of the beam pipe), so that x may be interpreted as the displacement of the center of a bunch slice. We also assume a bunch length much less than the betatron wavelength, therefore the displacement in the rhs of Equation (1) is not retarded and, finally, we use an average transverse wake function obtained from the wake of a single cavity [3], over the linac length.

We first consider the effect associated with a displacement of the electron bunch at the injection into the perfectly aligned linac. We then extend the analysis to the case of misalignments of the linac rf cavities and cryomodules.

Throughout the report we compare the results obtained to the output of a simple tracking code, written as a Mathematica notebook (See BBU tracking code description in Appendix A of this Chapter).

In order to keep the analytical expressions reasonably simple, we model the linac length as entirely filled with rf cavities (thus neglecting all the drift spaces that account for as much as one fifth of the total length). This causes the wakefield intensity used in the analysis to be larger than the actual value and the average accelerating gradient to be smaller. It can be shown that this corresponds to a conservative estimate of the BBU growth. When comparing the analytical results to MERLIN output (c.f Figure 4-9) it must be kept in mind that the *packing factor* is only 80%. Since the formulas we are going to derive next depend on the square for the linac length, we add a correction factor of ~0.64.

Since there are in focussing elements on the recirculated accelerating section, the solution of Equation (1) can be obtained using a perturbation technique. The first order solution $x_{(1)}$, with initial conditions: $x(s=0)=x_0$, $x'(s=0)=x'_0$ for all the electrons in the bunch, is [4]:

$$x_{(1)} = x_0 + x_0 A_0 \left[\frac{\Delta\gamma}{\gamma_i}\frac{s}{L} - \ln\left(1+\frac{\Delta\gamma}{\gamma_i}\frac{s}{L}\right)\right] + x'_0 L \frac{\gamma_i}{\Delta\gamma}\ln\left(1+\frac{\Delta\gamma}{\gamma_i}\frac{s}{L}\right) \tag{2}$$

where

$$A_0(z) = \frac{r_0\gamma_i L^2}{\Delta\gamma^2}\int_z^\infty \rho(z')W_\perp(z'-z)dz' \tag{3}$$

and L is the linac length, γ_i the injection energy and $\Delta\gamma$ the total energy gain accumulated up to s (i.e. taking into account eventual prior passes in the linac).

It is convenient to examine in detail the cases of coordinate and angular displacement at injection separately. For the numerical results the wake for the TESLA rf cavities [5] and a gaussian bunch (σ= 2 ps) are considered, but the formulas obtained below are valid for an arbitrary bunch distribution.

Coordinate Displacement and No Angular Displacement*: $x(s = 0,z)= x_0$, $x'(s = 0,z) = 0$.*

If we assume no angle error at injection Equation (2) becomes at the end of the *n-th* linac pass
($s = nL$)

$$\frac{x_{(1)}}{x_0} = 1 + A_0\left[\frac{\Delta\gamma}{\gamma_i} - \ln\left(1+\frac{\Delta\gamma}{\gamma_i}\right)\right] \tag{4}$$

Figure 4-1 shows the relative displacements, $x_{(1)}/x_0 - 1$, along the bunch, with respect to the bunch head, at the end of each pass in the linac, which is the source of vertical emittance growth.

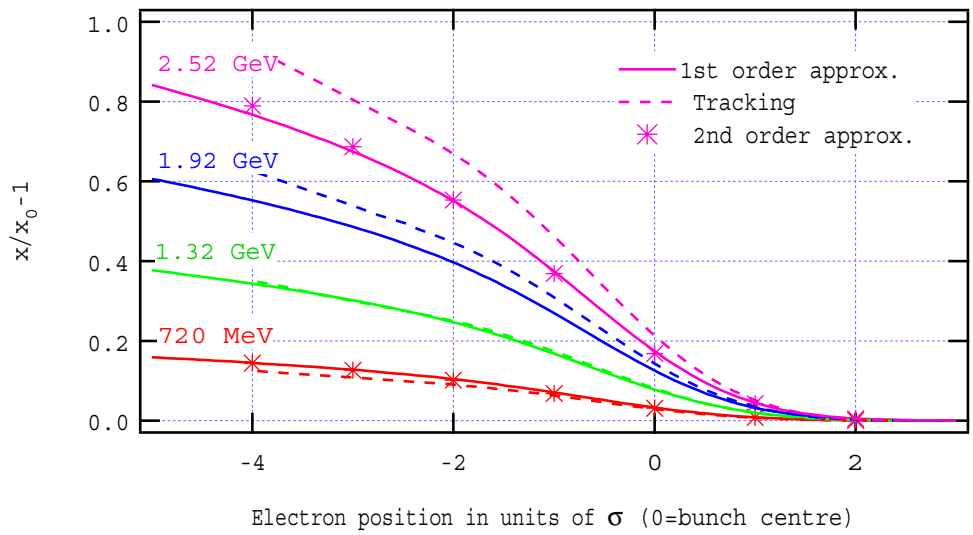

Figure 4-1 Cumulative transverse displacement (relative to the bunch head), as a function of the electron position within the bunch, after each pass, for coordinate displacement x_o at the entrance to the linac.

After the first pass the bunch tail is displaced by almost 20% of its initial displacement at injection with respect to the bunch head. As this value is non negligible, we also obtained the second order solution of Equation (1), to verify that the iterative method converges rapidly and that the first order solution is already adequate. The values obtained, at several positions along the bunch, are shown by asterisks in Figure 4-1. We conclude that the first order approximation can be safely used. In this model the beam transports directly from the end of the linac back to the beginning, and so additional passes are equivalent to having a longer linac. The second order approximation at the highest energy begins to be somewhat different from the first order result.

The dashed curves in Figure 4-1 are the output from our tracking code. The agreement between the analytical formula and the tracking code becomes worse at higher energies, corresponding to a longer linac, where the effect of the approximation made in the analysis become appreciable.

Figure 4-2 shows the transverse displacement at the end of the four linac passes for two different bunch lengths (1.5 and 3 mm) and two different charge distributions (gaussian and uniform). There are no significant differences in effects between the two distributions for a given bunch length, while the effect of the bunch length itself is substantial.

Angular Displacement and No Coordinate Displacement: $x(s = 0,z) = 0$, $x'(s = 0,z) = x'_0$.

In this case, the second order solution must be applied to improve our approximation:

$$\frac{x_{(2)}}{x_0' nL} = \frac{\gamma_i}{\Delta\gamma}\ln\left(1+\frac{\Delta\gamma}{\gamma_i}\right) + A_0\frac{\gamma_i}{\Delta\gamma}\left[\left(2+\frac{\Delta\gamma}{\gamma_i}\right)\ln\left(1+\frac{\Delta\gamma}{\gamma_i}\right) - 2\frac{\Delta\gamma}{\gamma_i}\right] \tag{5}$$

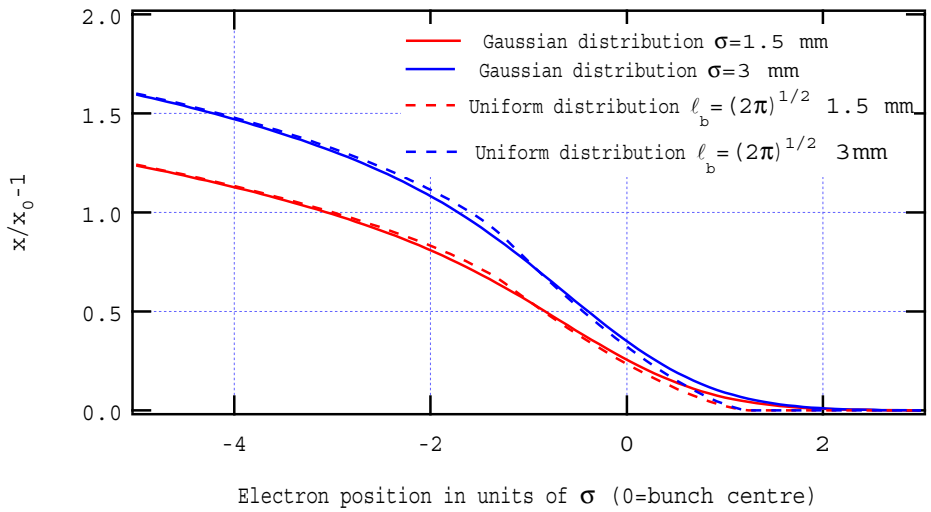

Figure 4-2 Displacement at the end of four passes for different bunch lengths and distributions, for coordinate displacement x_o at the entrance to the linac.

Figure 4-3 shows numerical results for the baseline parameters. The vertical axis shows the transverse position of the center of charge of each transverse slice along the bunch, with respect to the bunch head.

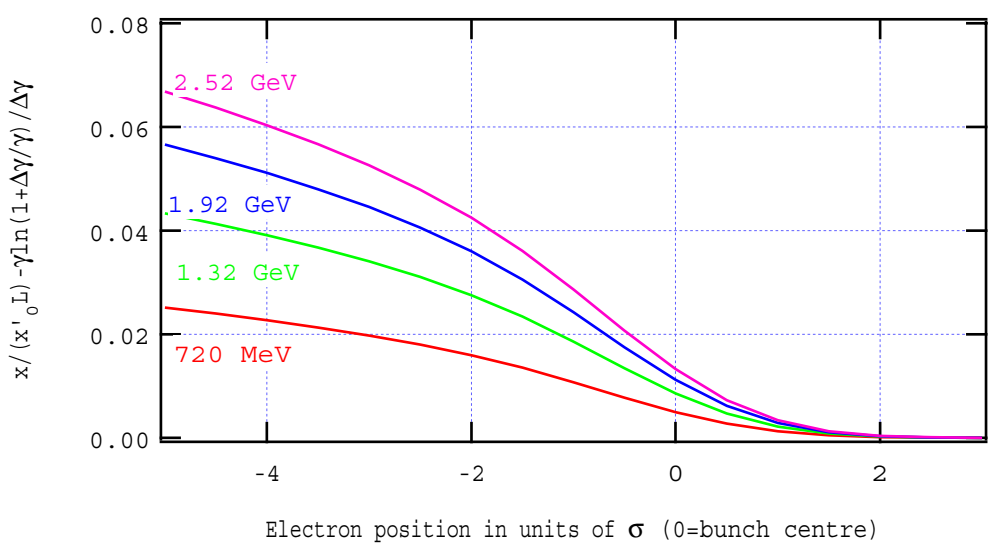

Figure 4-3 Electron displacement as a function of the position within the bunch (relative to the bunch head), for angular displacement x'_o at the entrance to the linac.

Comparing Figures 4-1 and 4-3, we observe that the effect of an angle error seems less significant than that of an injection offset, and this difference becomes more pronounced at higher energies.

Misalignment Effects

In the previous section it was assumed that the accelerator structure is perfectly aligned and the wake field is produced as a consequence of beam injection with a displacement or angle error. In this section the effects of misalignments of the rf cavities and cryomodules on the transverse dynamics is presented.

To begin with, consider only errors in the cavity alignment. This appears as an extra term on the rhs of Equation (1):

$$\frac{d}{ds}\left[\gamma(s)\frac{dx}{ds}\right]+k^2(s)\gamma(s)x(s,z)=r_0\int_z^{\infty}\rho(z')W_{\perp}(z'-z)\left[x(s,z')+d_c(s)\right]dz' \tag{6}$$

where the function $d_c(s)$ describes the misalignment, referred to an ideally perfectly aligned linac. We can again find an iterative solution of Equation (6) which, to first order, yields:

$$x_{(1)}(s,z)=x_0+A_0\left\{x_0\left[\frac{\Delta\gamma}{\gamma_i}\frac{s}{L}-\ln\left(1+\frac{\Delta\gamma}{\gamma_i}\frac{s}{L}\right)\right]+\sum_{i=0}^{N_{cav}-1}d_{ci}F_i(s)\right\}+x_0'\ln\left(1+\frac{\Delta\gamma}{\gamma_i}\frac{s}{L}\right) \tag{7}$$

where the functions $F_i(s)$ can be analytically calculated [4] and take into account the influence of the various cavity misalignments, depending on their respective position along the linac.

From Equation (7) we can see that the effect of cavity misalignments is to introduce an additional displacement that, in first approximation, does not depend on the injection coordinates x_0 and x_0'. Knowing the rms cavity misalignment, the wakefield-induced rms displacement can be calculated. Choosing $x_0=x_0'=0$, for example, we find:

$$\left\langle x^2\right\rangle^{1/2}=A_0(z)\sqrt{\sum_{i=0}^{N_{cav}-1}F_i(s)\left\langle d_c^{\,2}\right\rangle}^{1/2} \tag{8}$$

In calculating Equation (8), we have assumed no correlation between the alignment errors and this is strictly valid only when analyzing a single pass.

We can also account for the misalignments between the cryomodules in the same way finding equations analogous to Equations (6-8), but with the number of cryomodules N_{mod} and their length in place of the rf cavity number and length. Taking into account both alignment errors, Equation(8) becomes

$$\left\langle x^2\right\rangle^{1/2}=A_0(z)\sqrt{\sum_{i=0}^{N_{cav}-1}F_i(s)\left\langle d_c^{\,2}\right\rangle+\sum_{i=0}^{N_{\mathrm{mod}}-1}G_i(s)\left\langle d_m^{\,2}\right\rangle} \tag{9}$$

where the functions $G_i(s)$ are analogous to $F_i(s)$, but for cryomodules rather than for individual cavities.

We obtain for the first pass in the main linac, at the bunch center:

$$\left\langle x^2(z=0)\right\rangle^{1/2} \approx 0.0135\sqrt{\left\langle d_c{}^2\right\rangle + 7.74\left\langle d_m^2\right\rangle} \tag{10}$$

For the baseline parameters, and using 500 and 150 μm rms misalignments for the rf cavities and cryomodules respectively [5,6], Equation (10) yields a value of less than 10 μm for the rms transverse displacement of the electrons at the bunch center after the first linac pass.

In Figure 4-4 we compare Equation (10) with the tracking code output for several other misalignments values, finding a fairly good agreement.

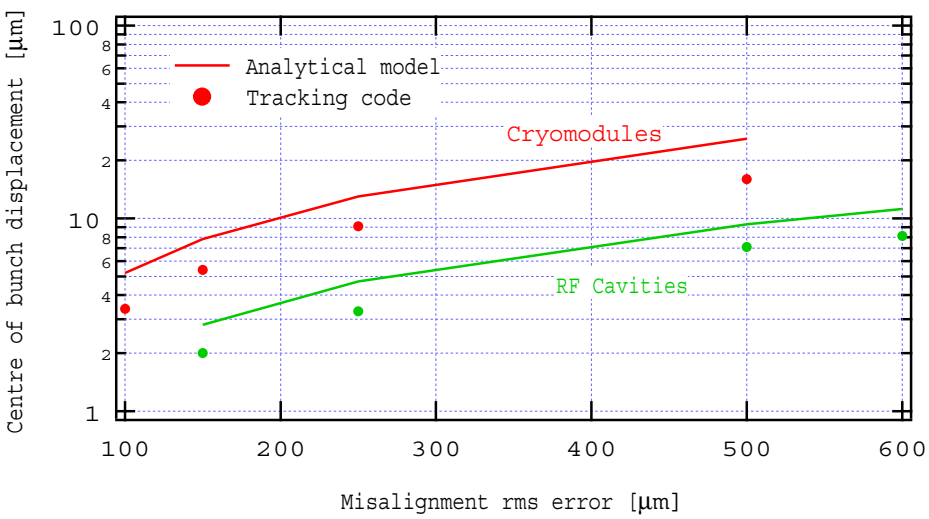

Figure 4-4 RMS value of the transverse displacement at the bunch centre (z = 0) as a function of rf cavities and cryomodules misalignments, after the first linac pass.

A direct consequence of Equation (7), when the cryomodule misalignments are taken into account as well, is that it is possible to cancel the effect of misalignments, at the linac exit, by choosing an opportune value for the initial displacement:

$$x_0 = -\frac{\sum_{i=0}^{N_{cav}-1} d_{ci}F_i(L) + \sum_{j=0}^{N_{mod}-1} d_{mj}G_j(L)}{\Delta\gamma/\gamma_i - \ln(1+\Delta\gamma/\gamma_i)} \tag{11}$$

This value can only be measured, after the linac has been assembled and aligned, by direct measurements of the beam profile. For baseline machine parameters, we expect the required offset to be in the range of 50 to 100 μm.

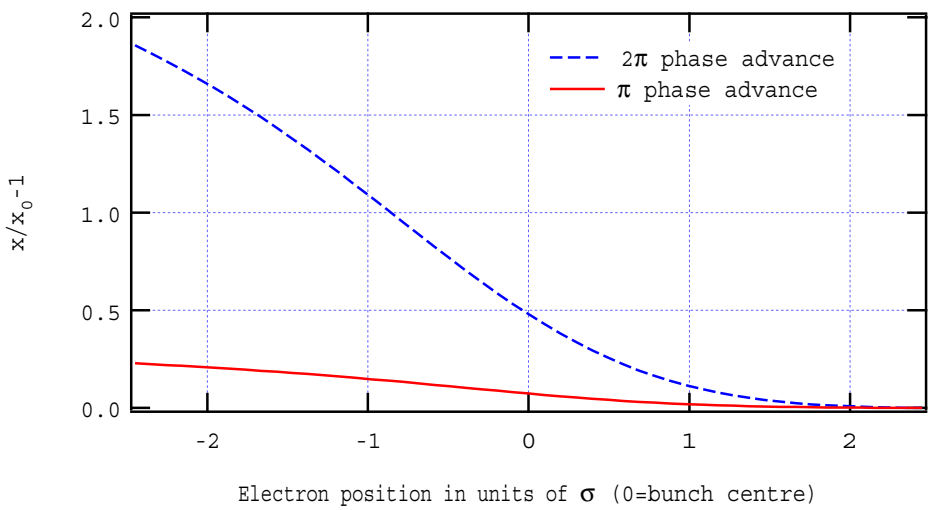

Figure 4-5 Electron displacement for zero betatron phase advance in all arcs (dotted line) and when the first arc has a π phase advance, for coordinate displacement x_o at the entrance to the linac.

It is also possible to design the arcs in such a way that the subsequent linac passes will have a canceling effect on the (strongest) displacement introduced in the first pass. Figure 4-5 shows the result from the tracking code with a betatron phase advance of π in the first return path and 2π in the subsequent return paths as opposed to the case of 2π phase advance in all four return paths. The results are calculated using a numerical tracking code with a 500 μm rms displacement error in the cavities and cryomodules and a 50μrad exit-entrance tilt error in the cryomodules. The improvement can be explained by the fact that changing the sign of the betatron phase along the bunch after the first turn inverts to displacement of the bunch and results in subsequent wakefields acting to reduce the transverse displacement generated in the first pass.

LONG-RANGE WAKEFIELDS

Because electron bunches are recirculated several times through the main linac, the effects of long-range wakefields stored in the rf cavity high order modes (HOM) has also been investigated. Data for the TESLA cavities HOM can be found in [5]

In general, the transverse wake field for a resonant mode is given by

$$w_{\perp}(t) = \frac{2c}{\overline{\omega}} \frac{k_{i\perp}}{b^2} e^{-t/\tau} \sin(\overline{\omega} t) \tag{12}$$

where b is the beam pipe radius, $k_{i\perp}$ is the transverse kick factor of the i-th mode, $\tau = 2Q/\omega$ and $\overline{\omega} = \sqrt{\omega^2 - 1/\tau^2}$.

The total transverse wake field is simply the sum of contributions from all the HOMs:

$$w_{\perp,tot}(t) = \sum_{i=1}^{N_{\text{hom}}} \frac{2c}{\overline{\omega}_i} \frac{k_{i\perp}}{b^2} e^{-t/\tau_i} \sin(\overline{\omega}_i t) \tag{13}$$

Given the high Q values, even for the damped modes, of order 10^4, with filling times of order microseconds, this field is not appreciably damped in the time it takes a bunch to re-enter the linac (<1 μs). The wakefields from different passes add up, and we can write the total wakefield at time t, with T_p the difference between the current time t and the time of the pth passage:

$$w_{\perp,tot}(t) = \sum_{i=1}^{N_{\text{hom}}} \frac{2c}{\overline{\omega}_i} \frac{k_{i\perp}}{b^2} \sum_{p=1}^{N_{pass}} e^{-(t+T_p)/\tau_i} \sin\left[\overline{\omega}_i \left(t + T_p\right)\right] \tag{14}$$

Figure 4-6 shows the typical long range transverse wake after a bunch first passage in the linac. A random detuning of ±0.1% between cavities has been taken into account, in the same way as done in the TESLA design report [5]. On its second pass the bunch will experience this wake value for $t = T_1$ and leave an identical wake, shifted in time by $t = T_1$. The sum of these two wakes, calculated in $t = T_2$, is the wake experienced by the bunch on its third pass and so on.

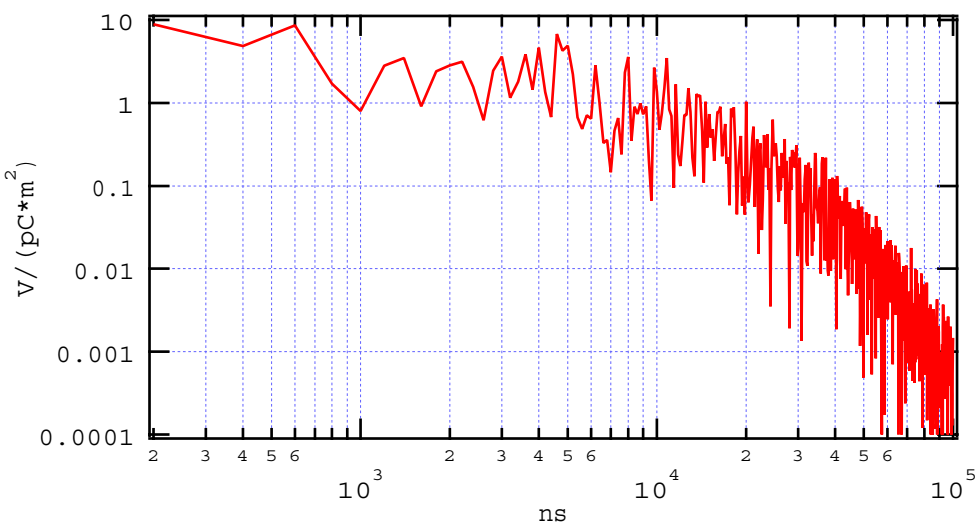

Figure 4-6 Transverse long-range wake averaged over 32 cavities with a frequency spread of ±0.1%.

Since the single-pass wakefield oscillates rapidly, its amplitude, as experienced by a bunch, depends on the exact time of passage. Even though later passes experience a sum of the wakes left from all the preceding passes, the oscillations in amplitude make it so that a bunch is not guaranteed to encounter a higher wake on a later pass, rather than on a previous one. We can see that the worst case is still that of the lowest energy pass, where the bunch is most sensitive to the transverse wake action.

The wake has sufficient time to decay to a negligible level when bunches are injected at the 10 kHz rate, and the long-range wake amplitude is fairly constant over the design bunch length of a few picoseconds.

Figure 4-7 shows a comparison of typical short and long range transverse wakefields for a 2 ps long bunch. It can be seen that the long range wake results in a small offset of the entire bunch. This also indicates that the amplitude of the long-range transverse wakefield is, generally, much smaller than the short-range one.

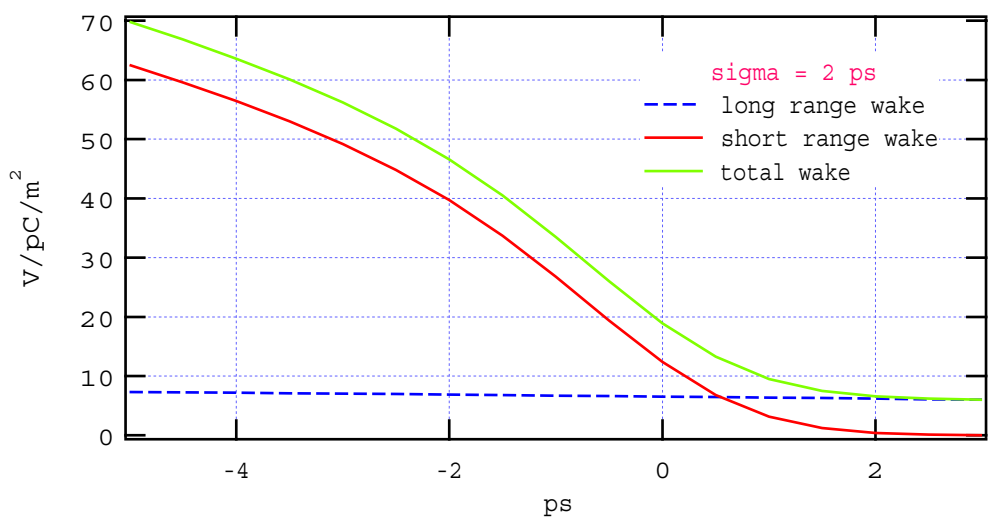

Figure 4-7 Short and long range transverse wakefields for a 2 ps long bunch.

INJECTOR LINAC

Before injection into the main linac, the electron bunch is accelerated from 10 to 120 MeV in an injector linac. This pre-accelerator is composed of a single cryomodule of the same kind as in the main linac. Therefore we will assume that the wake fields are the same and use the same formulae already derived for the main linac, but with different linac length (8.0 m), injection energy and energy gain. An important difference with the main linac is that, due to the lower energy, the bunch is subject to the focussing effect from the RF field [7]. This effect is included in Equation (1), when there are no other focussing elements, by writing:

$$k^2 = \frac{1}{2}\left(\frac{r_0 G}{e\gamma}\right)^2 \tag{15}$$

where $G \approx 14$ MV/m is the average accelerating gradient in the pre-accelerator.

Given the high relative energy change of a factor 12 from injection to extraction, the betatron wavelength changes from 4.83 m at injection to 31.4 m at the end of the injector linac.

Under these conditions, Equation (1) can no longer be solved analytically. Therefore, we check that in the absence of focussing the wake field effect is still below the maximum allowed. This will be a conservative estimate since focussing can only help control the BBU growth.

From Equation (4) it is readily seen that the bunch center transverse displacement at the end of the linac, for a 2 ps bunch, is

$$\frac{x(z=0)}{x_0} \approx 2.4\ 10^{-3} \tag{16}$$

As, this is a small effect, it may be ignored.

LONGITUDINAL WAKEFIELD

The voltage associated with the longitudinal wakefield in the main linac can introduce energy spread within a bunch. A classic remedy to this effect is accelerating the bunch off the rf wave crest, choosing an appropriate phase such that the variation of the main rf voltage along the bunch counterbalances the wakefield voltage.

We can write the rf voltage experienced by a particle inside the bunch as:

$$V_{RF}(\varphi_0, \tau) = \hat{V}_{RF} \cos(\varphi_0 + \omega_{RF}\tau) \tag{17}$$

where φ_0 is the bunch centre phase, with respect to the rf wave, $\hat{V}_{RF}$ is the RF peak voltage and ω_{RF} its angular frequency, τ indicates a particle position inside the bunch, τ = 0 corresponding to the bunch center.

The voltage from the longitudinal wakefield is written as:

$$V_W(s) = \int_{-\infty}^{s} \rho(s')w(s-s')ds' \tag{18}$$

where $\rho(s)$ is the bunch charge distribution, $w(s)$ the longitudinal wake function and s is the distance from the bunch center.

Since $s = c\tau$, the total voltage along the bunch is

$$V_{tot}(\varphi_0, \tau) = V_{RF}(\varphi_0, \tau) + V_W(\tau) \tag{19}$$

From its Taylor series expansion, about the bunch centre

$$\begin{aligned} V_{tot}(\varphi_0, \tau) &\approx V_{tot}(\varphi_0, 0) + \frac{\partial}{\partial \tau}\left[V_{tot}(\varphi_0, \tau)\right]_{\tau=0}\tau = \\ &= \hat{V}_{RF}\cos\varphi_0 + V_W(0) - \left(\omega_{RF}\hat{V}_{RF}\sin\varphi_0 - \frac{\partial}{\partial \tau}\left[V_W(\tau)\right]_{\tau=0}\right)\tau \end{aligned} \tag{20}$$

we see that canceling the term in between brackets would cancel the first-order dependence of the total voltage on the position inside the bunch. This means choosing a bunch center phase such that

$$\sin\varphi_0 = \frac{c}{\omega_{RF}\hat{V}_{RF}} \frac{\partial}{\partial s}\left(\int_{-\infty}^{s} \rho(s')w(s-s')ds'\right)_{s=0} \tag{21}$$

To calculate the integral in Equation (21) we use the following wake function:

$$w(s) = -38.1\left\lfloor \frac{V}{pC \cdot m} \right\rfloor \left(1.165\ e^{-\sqrt{s/3.65\,mm}} - 0.165\right) \tag{22}$$

given in [5] for the steady-state wake of a point charge. The use of the steady-state wake is justified for the main linac, but it is only approximately correct in the case of the shorter injector

linac. The uniform longitudinal charge distribution we use is defined as $\lambda(s) = Q_b / l_b$ in the interval $0 < s < l_b$, where Q_b is the bunch charge and l_b its length.

With these assumptions, Equation (21) yields an absolutely negligible value for the required rf phase, demonstrating that the longitudinal wakefield effect can be ignored in the main linac. For the case of the injector we find that timing jitter following the action of the bunch compressor require correction of the longitudinal wake effects in the injector linac up to the second order. To this end, using Equation (22) and the charge distribution defined above we calculate the electrons energy loss, as a function of their position in the bunch, using the following expression:

$$\frac{1}{Q_b}\frac{dE(s)}{dz} = -19.05\left[\frac{V}{pC\cdot m}\right]\int_{-1}^{2s/l_b}\left(1.165\ e^{-\sqrt{\frac{s-x(l_b/2)}{3.65\,mm}}} - 0.165\right)dx \tag{23}$$

We found that the right hand side of Equation (23) can be accurately described by a quadratic polynomial. For the injector linac, with a bunch length of 20 ps we obtain:

$$\frac{1}{Q_b}\frac{dE(s)}{dz} = \left[-9.32 - 6.34\left(\frac{2s}{l_b}\right) + 2.42\left(\frac{2s}{l_b}\right)^2\right]\left[\frac{V}{pC\cdot m}\right] \tag{24}$$

and for the main linac, with a 2 ps bunch length, we obtain:

$$\frac{1}{Q_b}\frac{dE(s)}{dz} = \left[-15.25 - 13.72\left(\frac{2s}{l_b}\right) + 1.33\left(\frac{2s}{l_b}\right)^2\right]\left[\frac{V}{pC\cdot m}\right] \tag{25}$$

Figure 8 shows plots of the two fitting functions given in Equations (25) and (25) (colored dashed curves). We also evaluate directly Equation (23) for the same bunch lengths (solid black curves) and found that the results are virtually indistinguishable.

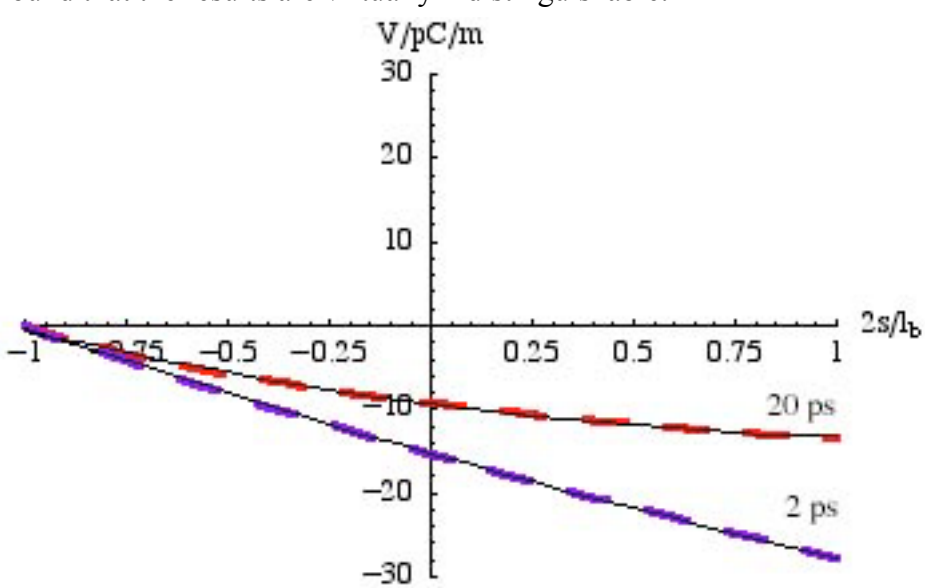

Figure 4-8 Energy loss of electrons, due to the longitudinal wake, for 2 ps and 20 ps bunches.

TRACKING STUDIES

In addition to analytical estimates a more complete investigation including the nominal bunch distribution and tracking through the arcs has been made using a tracking code. For the present studies, we have used MERLIN [8], which allows the simulation of all the required effects.

Linac Tracking

The present design of the linac uses the TESLA 9 cell, 1.3 GHz superconducting cavities [4]. These are standing wave structures, for which the transfer map (the Chambers' Matrix) is known [9]. The fringe-field focusing is included in this transfer map, and although the exit field of one cavity is (approximately) cancelled by the entrance field of the following cavity, the exit and entrance fields of the whole linac do not cancel because of the gain in energy through the linac. This effect is most significant in the first pass through the linac, since the relative gain in energy is large. There is an effect on the linear optics from the fringe-field focusing; this has been included in the lattice design produced using MAD 8acc [10]. The implementation of the transfer map in MERLIN differs in one respect from that in MAD 8acc, namely the MERLIN map includes a transverse focusing from the RF in the body of the cavity, which is negligibly small in the parameter regime (cavity parameters and beam energy) of the femtosecond light source. This term is omitted in the MAD 8acc map [11]. The Chambers' Matrix gives the correct adiabatic damping of the transverse and longitudinal emittances.

It is assumed that the orbit through the linac can be controlled to the level of a few tens of microns. The main contribution to the wake fields then comes from misalignments of the cavities. The specified vertical alignment tolerance of the cavities in the linac is 500 μm rms within a cryostat, and 150 μm rms between cryostats. The lattice model is constructed in MERLIN in such a way that the beam sees the same set of misalignments on each pass through the linac.

The wake fields are implemented in the standard way for macroparticle tracking codes. Specifically, the macroparticles are binned to determine the longitudinal distribution, and an appropriate kick is determined for each macroparticle by forming the convolution of the distribution with the specified Green's function. In MERLIN, any number of steps can generally be taken through beamline components, with processes such as wake fields applied at the end of each step. However, a limitation specific for a standing wave cavity, is that the transfer map is valid only for a cavity consisting of an integer number of cells. In the present simulation, each cavity is treated as a sequence of nine cells with zero separation between; wake field kicks were therefore applied nine times for each cavity.

Arc Tracking

Symplectic tracking is implemented for standard (non-accelerating) beamline components. Nonlinear components such as sextupoles can be treated in various approximations; for the present studies, they were treated in the thin-lens approximation. The symplectic condition ensures that no spurious emittance growth or damping is introduced.

The lattice design uses sextupoles to minimize the second-order dependence of time-of-flight on energy. Although the sextupole strengths are not great, vertical beam offset in the sextupoles could have a significant impact on machine performance through the coupling of horizontal emittance into the vertical plane. Even if the beam was injected on the design orbit into the linac for these simulations, the fringe fields and wake fields from misaligned cavities lead to orbit distortion. To separate the emittance growth from wake fields and sextupoles, we simply compare the results of tracking with and without sextupoles. In the latter case, there is an effect on the bunch length, with a longitudinal tail that is not expected to affect the results significantly. Note that the map for a dipole implemented in MERLIN includes second-order terms that can also give betatron coupling; some vertical emittance growth is therefore expected even with the sextupoles turned off, though this should be much less than the coupling resulting from the sextupoles. Below, the emittance growth in several situations, with wake fields and sextupoles turned on and off in various combinations, is compared.

The arcs include a phase trombone to allow control over the betatron phase advances. It is possible, for example, that there may be benefits to having half-integer phase advances over each arc. For the present studies, although the arcs were not specially tuned, the vertical phase advance over each arc was close to a half integer. This means that the wake field kicks on successive passes will nearly cancel.

Benchmarking Wake Field Simulations

To verify the wake field model in MERLIN, a bunch with nominal 2 ps bunch length, and (effectively) zero transverse emittance was first tracked through four passes of the linac. In this case, the bunch was injected so as to have a fixed vertical offset in each cavity, and the bunch was taken straight from the end of the linac on each pass and re-injected at the start of the linac: i.e. modeling the effects of perfectly achromatic arcs with integer betatron phase advances. This system has been studied semi-analytically and reported earlier, and provides a benchmark for the wake field model in our MERLIN simulations.

The results of the simulation are shown in Figure 4-9, tracking a bunch with the nominal 1 nC charge, consisting of 10,000 macroparticles: the macroparticles are somewhat sparse at the 3 sigma tails of the distribution. The vertical axis is normalized, so that the transverse deflection is expressed as a fraction of the initial bunch offset. In the previous analysis, it is assumed that the length of the linac is filled with structures, whereas the packing factor is actually about 80%. Once this factor is taken into account, there is excellent agreement between the results of Figure 1 and the results shown in Figure 4-9.

It should be noted that the 35% deflection after four passes observed in Figure 4-9 represents an extremely pessimistic case. With random misalignments, there will be significant cancellation between the wake fields of different cavities (aside from pathological cases). In addition, the phase advance over the arcs mentioned above will tend to cancel the effects of the kicks on successive passes.

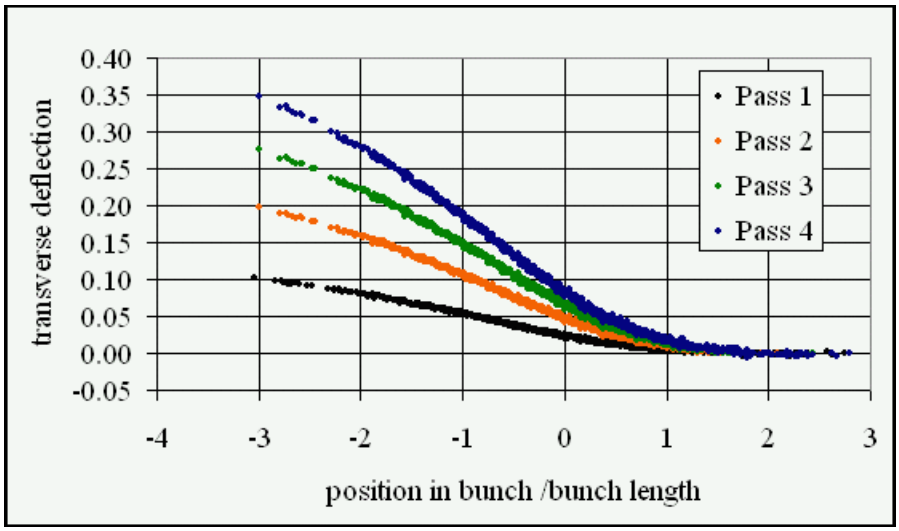

Figure 4-9 Transverse deflections of a 2 ps zero-emittance beam, after four consecutive passes at constant vertical offset through the linac.

Vertical Emittance Growth

To estimate the emittance growth from the wake fields in a linac with vertical cavity misalignments, a bunch (of 10,000 macroparticles) was tracked with the nominal parameters as specified in Table 4-1 from the entrance to the linac to the exit after the fourth pass. Vertical misalignments with a range of rms values (and a cut-off at 5 sigma) were applied to the cavities; as mentioned above, the beam sees the same misalignments in the simulation on each pass. The cavity misalignments were the only imperfections applied to the machine; the arc optics and alignment were as designed. For large cavity misalignments, there is significant orbit distortion that is expected to lead to vertical emittance growth from coupling in the arc sextupoles. No distinction was made between cryostats; in reality, cavity offsets are expected to be correlated according to which cryostat they are in. Since we find that the wake field effects for any reasonable cavity misalignments are so small, our conclusions are not likely to be affected by the fact that we have neglected this effect.

Table 4-1 Bunch parameters used in wake field simulations

Initial bunch energy	120 MeV
Bunch charge	1 nC
Bunch length	2 ps
Energy spread	10^{-3}
Horizontal emittance (normalized)	20 μm
Vertical emittance (normalized)	0.4 μm

Results of tracking with the sextupoles turned on are shown in Figure 4-10; results with the sextupoles off are shown in Figure 4-11. Each figure shows the results of 200 seeds (the same seeds for each data series) of cavity misalignments with rms varying from zero up to 2 mm. Note the different vertical scales in the two graphs, and that the vertical misalignment scale (horizontal axis) extends an order of magnitude beyond the specified alignment tolerance on the cavities.

It appears that the wake fields make negligible contribution to the emittance growth as can be shown with a simple estimate based on the results shown in Figure 4-9. For the mean vertical displacement we take the largest rms cavity misalignment divided by the square root of the number of cavities in the linac (the linac is composed of 32 cavities). The displacement between the head (+1 sigma) and the tail (-1 sigma) of the bunch after the fourth pass, given no phase advance over the arcs, is of the order 15% of the mean cavity misalignment. For 2 mm rms (and hence 350 µm mean) cavity misalignment, we expect a vertical displacement of the bunch tail with respect to the head of about 50 µm. This is to be compared with the bunch size of 70 µm at the end of the fourth pass of the linac. The wake field cancellation resulting from the phase advance across the arcs can easily reduce the head-tail displacement by more than an order of magnitude; in which case, we would expect to see an emittance growth of the order 5% (with 2 mm rms vertical cavity misalignment). From Figure 4-11, it appears the wake fields make an even smaller contribution to the vertical emittance; we note that the mean cavity misalignment in our simulations is actually closer to 100 µm than 350 µm (statistical fluctuations) when the rms cavity misalignment is around 2 mm.

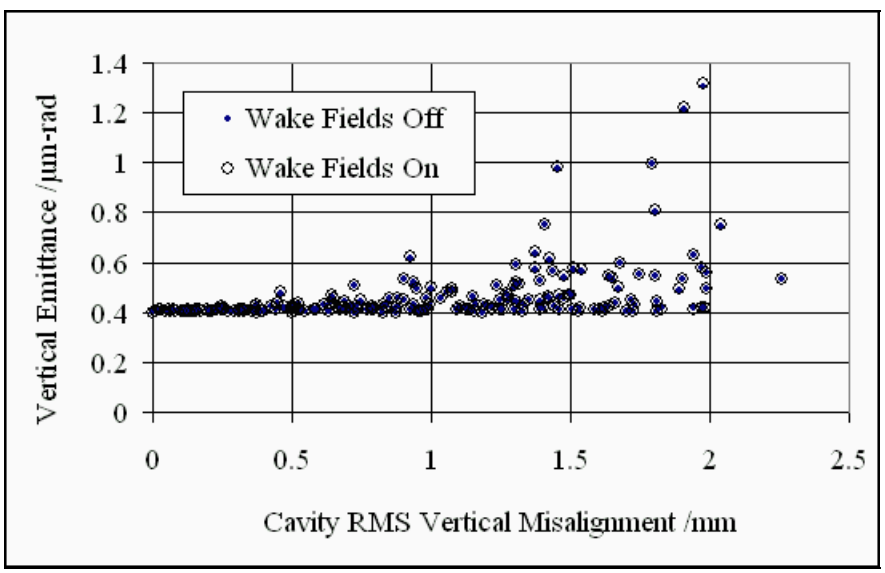

Figure 4-10 Results of tracking a nominal bunch from the first entrance of the linac through four passes (including the arcs) to the fourth exit from the linac. The arc sextupoles were turned on.

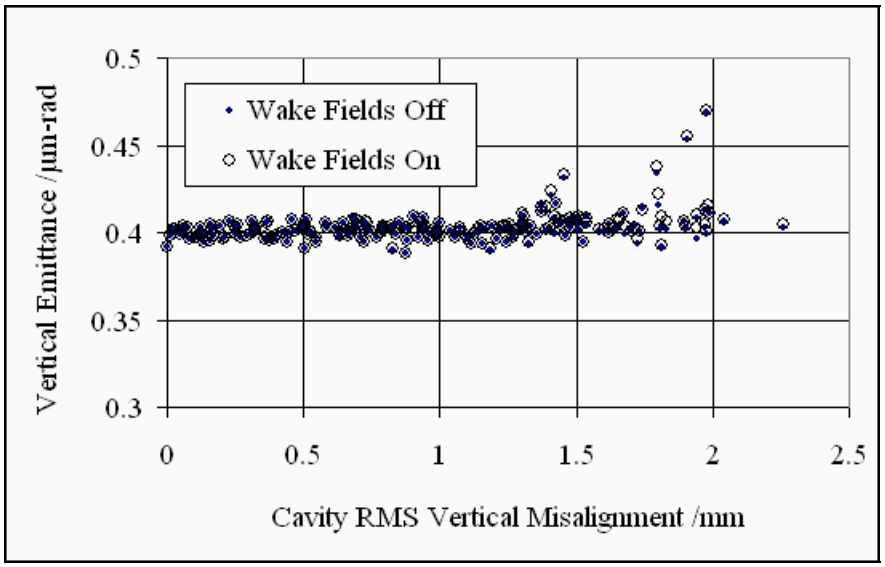

Figure 4-11 Results of tracking a nominal bunch from the first entrance of the linac through four passes (including the arcs) to the fourth exit from the linac. The arc sextupoles were turned off.

With the sextupoles turned on, any emittance growth from the wake fields is hidden by the very much larger emittance growth from the coupling. This should be easily fixed by proper orbit control.

The results of our simulations of emittance growth resulting from wake fields in the rf cavities are broadly consistent with rough estimates, based on knowledge of the wake field effects in the case of a constant beam transverse offset in the linac. For any reasonable cavity alignment (a few hundred microns rms with respect to the design orbit), the emittance growth from wake fields in the cavities is small. Controlling the orbit in the sextupoles to avoid emittance growth from betatron coupling is a more significant issue.

Figure 4-12 shows how the vertical-longuitudinal correlation, introduced by the wake fields, is negligible even when no coupling is present (sextupoles off).

RESISTIVE WALL IMPEDANCE

The transverse wakefield from the resistive wall impedance for a circular pipe of radius b, length L, electrical conductivity σ_c is given in *V/pC/m* by [12]:

$$W_1(z) = \frac{c\,L}{\pi\,b^3}\sqrt{\frac{Z_0}{\pi\,\sigma_c}}\;\frac{1}{\sqrt{z}} \tag{26}$$

For a charge distribution $\rho(z')$ the wake is then:

$$W_1(z) = \frac{c\,L}{\pi\,b^3}\sqrt{\frac{Z_0}{\pi\,\sigma_c}}\int_{-\infty}^{z}\rho(z')\,\frac{dz'}{\sqrt{|z-z'|}} \tag{27}$$

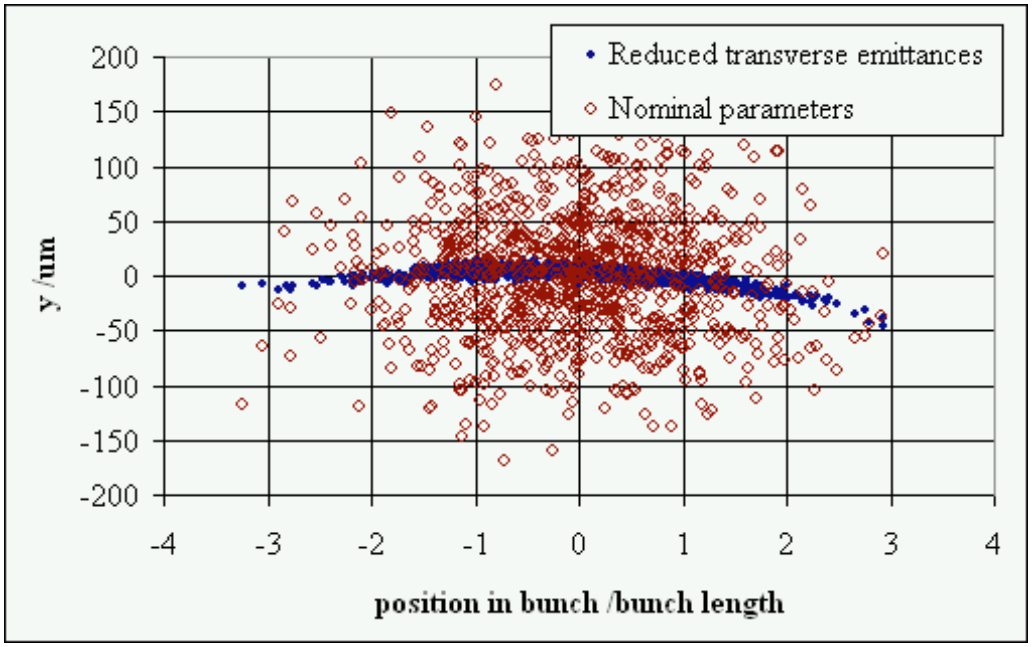

Figure 4-12 Results of tracking two bunches four passes through the linac and arcs. The cavities were misaligned with rms 2 mm and mean 350 mm, and the sextupoles were turned off. The vertical-longitudinal correlation introduced by the wake fields is visible when the transverse emittances are reduced (by six orders of magnitude), but the effect on the nominal bunch is negligible.

which, for a Gaussian bunch of unit charge becomes:

$$W_1(z) = \frac{c\,L}{\pi\,b^3}\sqrt{\frac{Z_0}{\pi\,\sigma_c}}\;\frac{1}{\sigma_z\sqrt{2\pi}}\int_{-\infty}^{z} e^{-\frac{z'^2}{2\,\sigma_z^2}}\;\frac{dz'}{\sqrt{|z-z'|}} \tag{28}$$

The deflecting voltage for a bunch of N particles of charge e and offset y_0 is therefore:

$$V_\perp(z) = N\,e\,y_0\,W_1(z) \tag{29}$$

The angular deflection along a gaussian beam of energy E is given by:

$$\Delta y'(z) = \frac{N\,e\,y_0}{\frac{E}{e}}\,W_1(z) \tag{30}$$

Note that the resistive wall induced kick scales inversely with energy and the beamsize scales inversely with the square root of energy, thus the increase in projected emittance resulting from wakefield-induced distortions along the bunch is largest at low-energy.

Starting from the parameters of Table 4-2, wakefields are calculated solving the above expressions numerically for Gaussian bunches and similar expressions for a rectangular charge distribution. The resulting transverse deflection along the bunch is calculated for a unit length of beampipe.

Table 4-2 Baseline parameters for resistive wall calculations

Normalized vertical emittance $\gamma\varepsilon_v$	0.4 mm-mrad
ß-function $ß_v$	10 - 30 m
Beam energy (pass #)	Beamsize σ_v
120 MeV (0)	170 - 511 µm
710 MeV (1)	54 - 93 µm
1.3 GeV (2)	40 - 69 µm
1.9 GeV (3)	33 - 57 µm
2.5 GeV (4)	28 - 50 µm
Chamber radius	1.5 cm
Chamber length	1 m
Chamber conductivity	3.5×10^7 (Al)
Bunch offset	100 µm
Number of electrons (1nC)	6.24×10^9

We choose here aluminum vacuum chambers, although other materials may be considered, for example a copper ($\sigma_{Cu} = 5.6\times10^7$) vacuum chamber reduces the wakefield by 25%. A stainless steel ($\sigma_{St.\ St.} = 0.11\times10^7$) vacuum chamber, however, increases the effect by a factor 5.6.

First arc (710 MeV)

Figure 4-13 shows the resistive wall wakefield together with the charge distributions for gaussian and rectangular bunches in the first full arc at 710 MeV. The deflection angles for the same parameters are shown in Figure 4-14. These figures show that the typical "banana" shaped distribution along the bunch resulting from the short-range resistive wall wakefield. Figure 4-15 shows the deflection along a bunch as a function of the bunch length.

The displacement *y* along the bunch is calculated as the product of the deflection and the length of beampipe. Even for the case of a 1 ps rectangular bunch at 710 MeV, the deflection is 6.8×10^{-10} rad m^{-1} and the distortion at the end of a 2 ps, 1 nC, rectangular bunch arising from resistive wall transverse wakefields is 0.25 % of the vertical beamsize for a complete arc of 200-m length. For a 2 ps bunch at 3 nC, the distortion is 0.5%

The bunch distortion from the resistive wall wakefield is small in a 3 cm diameter aluminum beampipe under these conditions. For a 2 ps, 3 nC, bunch and allowing for ±250 µm closed orbit distortion, the vacuum chamber vertical alignment with respect to the quadrupole centers must be better than 1 mm. Wakefields arising from positive and negative offsets will tend to cancel each other, and an average integrated vacuum chamber (vertical) alignment of 1 mm gives a 5% distortion within a bunch after the first pass.

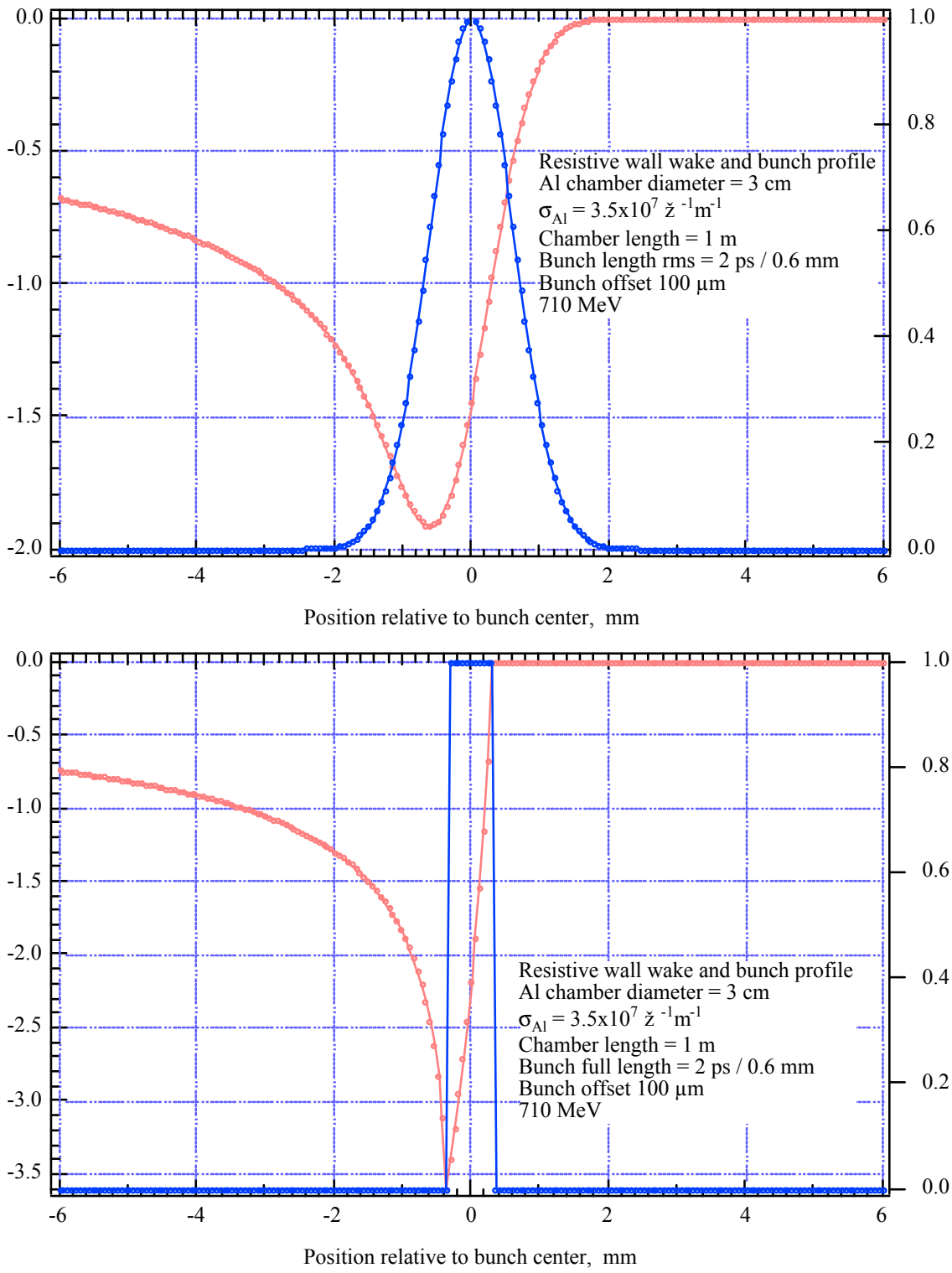

Figure 4-13 Charge distribution and resistive wall wake in the first arc, for gaussian (top), and rectangular (bottom) longitudinal distributions.

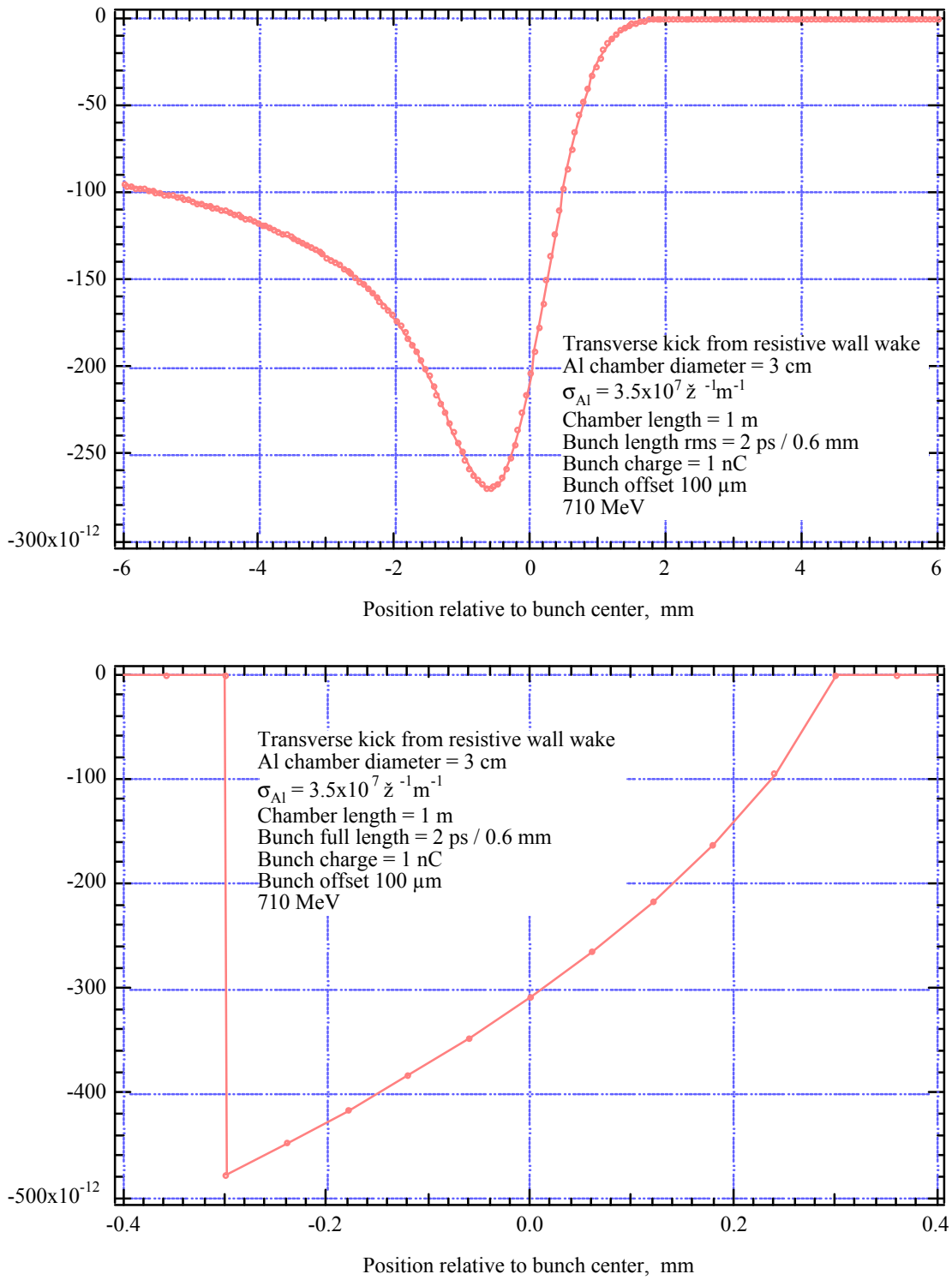

Figure 4-14 Transverse deflection (rad) for a 1-m long, 3-cm diameter vacuum chamber section in the first arc, for gaussian (top), and rectangular (bottom) longitudinal distributions.

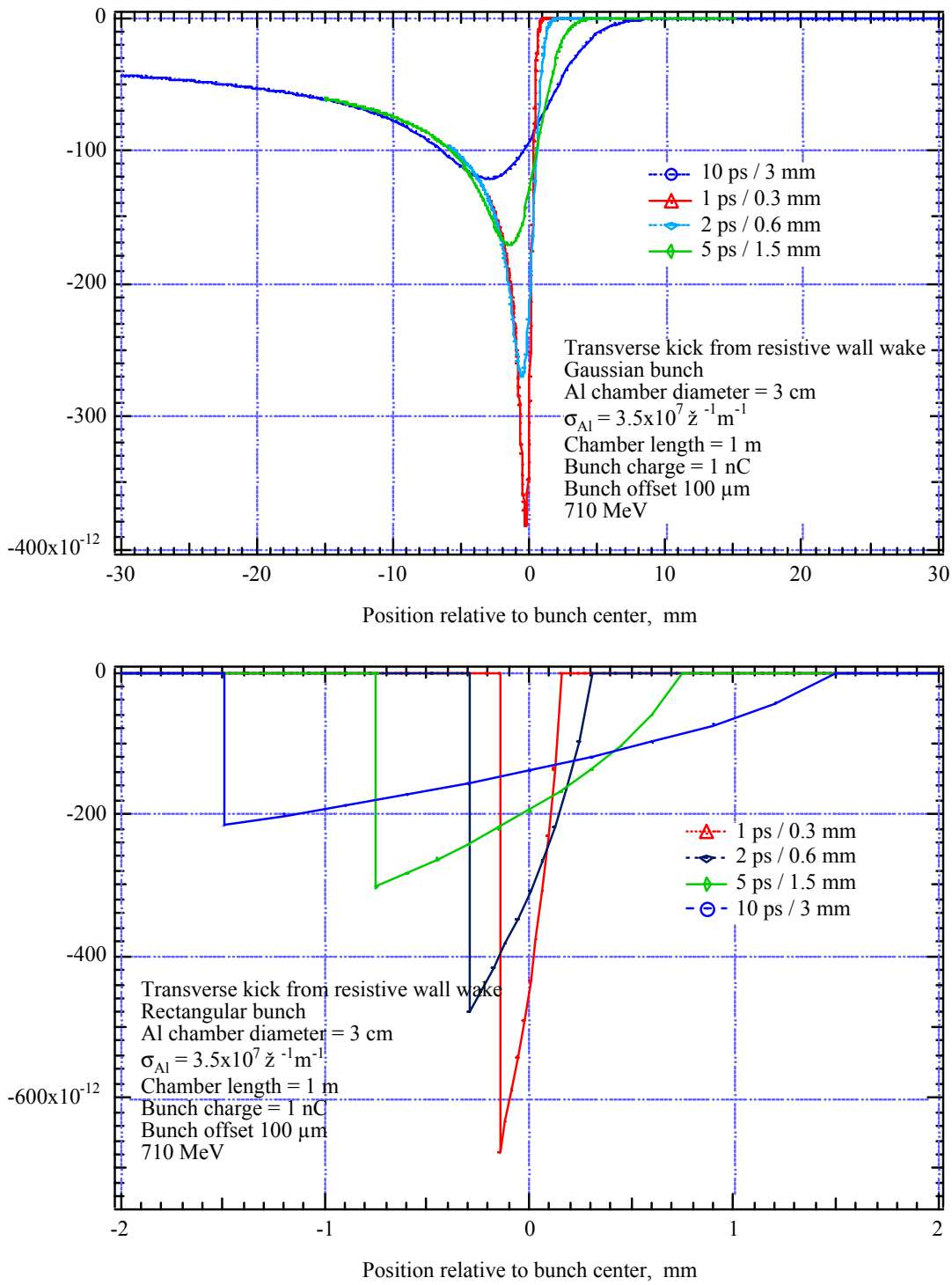

Figure 4-15 Deflection along bunches of 1 - 10 ps length with 1 nC charge, offset 100 µm, over 1 m of 3 cm diameter vacuum chamber at 710 MeV, for gaussian (top), and rectangular (bottom) longitudinal distributions.

Injection (120 MeV)

To shield from coherent synchrotron radiation effects in the low-energy beam passing through the Arc0 connecting the injector linac to the main linac, the vacuum chamber height is reduced to 5 cm (in the bending magnet sections only).

For a 3-m beampipe of 5-mm diameter, the distortion along the 2 ps, 3 nC, rectangular bunch with 100 μm offset is approximately 3% of σ_y. Such an aperture must be aligned to 100μm of the beam orbit.

Since the wake scales as $1/b^3$, an increase in beampipe diameter by a factor of 2 results in a factor 8 decrease in wakefield. A 9-mm diameter beampipe would require alignment to order 0.5 mm in the 120 MeV dipole magnets to maintain beamsize growth in this section less than 2%.

Photon production arc

Small-aperture undulators are used in the photon production section, and for a beampipe of 5 mm diameter at 2.5 GeV with a 2 ps, 3 nC rectangular bunch we find a distortion of approximately 6% σ_y over 20 m. The vacuum chamber dimensions should be opened up between insertion devices to reduce this effect. Operating with cold walls in the superconducting insertion devices will improve the situation.

COHERENT SYNCHROTRON RADIATION

Here we present preliminary estimates for a coherent synchrotron radiation (CSR) of electrons in the recirculating linac x-ray source. As described elsewhere [13-15], CSR causes energy loss of electrons and emittance increase in the orbit plane resulting from the energy loss to coherent synchrotron radiation emitted as a bunch passes through the bend magnets. Since the design horizontal emittance is relatively large, small additional emittance growth seems not to be harmful. Therefore, we are mainly concerned with the energy loss and its potentially adverse effect on production of short x-ray pulses through increased energy spread in the bunch.

The electron bunch length and energy varies as a function of location in the recirculating linac lattice, and in each of the several types of dipole magnets. In all cases, we are in the so-called *steady-state CSR* [15] regime defined as follows:

$$\varphi_m \geq \left(24 \frac{l_b}{\rho} \right)^{1/3} \tag{31}$$

where φ_m is the magnet arc angle, ρ is the bending radius, and l_b is the electron bunch length. When the above condition is met the magnet is sufficient long so that radiation emitted by particles in the tail catches and passes the particles at the head of a bunch before the bunch leaves the magnet. The CSR energy loss per unit length of trajectory can then be written as [13-15]:

$$\frac{dE(s)}{dz} \cong -\frac{2}{3^{1/3}\sqrt{2\pi}} \frac{Ne^2}{\sigma_0 \rho^{2/3}} \int_{-\infty}^{s} \left(e^{-\frac{s'^2}{2\sigma_0^2}} - e^{-\frac{(s'-l_b)^2}{2\sigma_0^2}} \right) \frac{ds'}{(s-s')^{1/3}}, \tag{32}$$

where N is a number of particles per bunch, and e is the electron charge. In deriving Equation (32), we assume a uniform longitudinal density distribution $\lambda(s) = N / l_b$ in interval $0 < s < l_b$ with smooth transitions at the edges with a characteristic length σ_0 as shown in Figure 4-16.

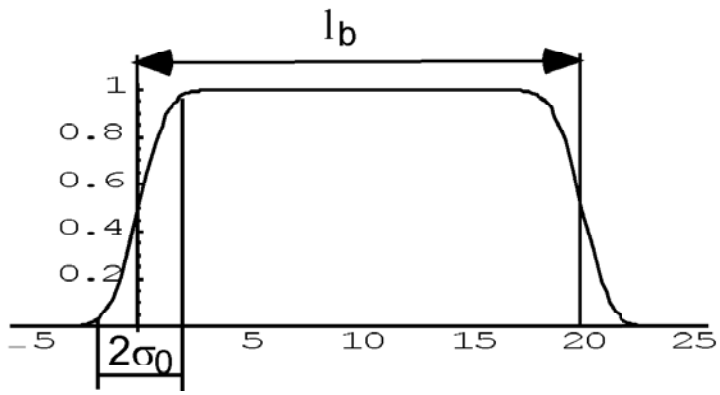

Figure 4-16 Longitudinal density profile of electrons in a bunch.

The integral in Equation (32) can be evaluated using analytical functions and the resulting function $dE(s)/dz$ is shown in Figure 4-17.

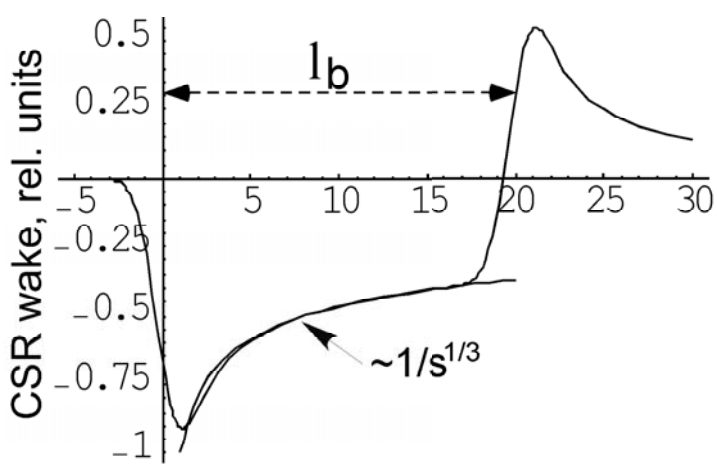

Figure 4-17 CSR wake function $dE(s)/dz$ for an electron longitudinal density distribution shown in Figure 15.

Note that $dE(s)/dz \sim 1/s^{1/3}$ over the entire length of the bunch excluding the edges. For this functional dependence one can consider partial compensation of the energy variation within the electron bunch induced by CSR, by using off-peak acceleration in the linac.

Using a $1/s^{1/3}$ dependence for the CSR wake function, one can calculate the average energy loss per electron due to the CSR in a magnet of length L_m for the main core particles with the expression [15]:

$$\Delta E = \frac{L_m}{l_b}\int_0^{l_b}\frac{dE(s)}{dz}\,ds \cong \frac{3^{2/3}Ne^2}{\rho^{2/3}l_b^{4/3}}\,L_m\,. \tag{33}$$

Table 4-3 lists CSR energy loss for all magnets at all beam energies and bunch lengths. The total energy loss is the so-called a *free-space* radiation. In practice, the electron bunch travels inside a vacuum chamber that acts as a waveguide for emitted radiation, and does not allow propagation of radiation below a geometry determined cut-off frequency. Thus, not all spectral components of CSR propagate in the vacuum chamber and the actual radiated energy is less than in the free space environment. For an estimate of the shielding effect of the vacuum chamber we follow the analysis suggested in [16]:

$$\Delta E_{\text{shielded}}/\Delta E_{\text{free space}} \cong 4.2\left(n_{th}/n_c\right)^{5/6}\exp\left(-2n_{th}/n_c\right)\ (n_{th} > n_c) \tag{34}$$

Here $n_{th} = \sqrt{2/3}\left(\pi\rho/h\right)^{3/2}$ is the threshold harmonic number for propagating waves, h is the height of the vacuum pipe assumed for the purposes of this calculation to be a parallel-plate, and $n_c = \rho/\sigma_c$ is the characteristic harmonic number for a gaussian longitudinal density distribution with the rms value of σ_c. The meaning of n_c is that the spectral component of radiation emitted with harmonic number beyond n_c is incoherent. We define $\sigma_c = l_b/3.22$, giving a good approximation of spectra for the uniform density distribution compared to the known spectra for a gaussian distribution. Table 4-3 shows two values of vacuum chamber height, h equal to 0.9 cm and 0.7 cm.

Table 4-3 Coherent synchrotron radiation energy loss in the dipole magnets for free space, 9 mm vacuum chamber, and 7 mm vacuum chamber as a function of beam energy.

Beam energy, MeV	120	120	120	720	1320	1920	2520	2520	2520
Bunch length, ps	20	2	2	2	2	2	2	2	2
Magnet length, cm	125.66	125.66	20.4	80	80	80	80	20	25.4
Magnet field, kG	3.33	3.33	6.4	11.12	10.23	9.93	10.56	9.54	20
Energy loss dE, keV	-19	-409	-103	-176	-111	-85	-74	-17	-36
# magnets	1	2	2	22	40	58	34	12	6
Free space energy loss, keV	-19	-818	-205	-3874	-4447	-4925	-2509	-207	-215
Shielded energy loss for vacuum chamber height:									
9 mm height, keV	0	-419	-147	-1209	-557	-291	-47	-6	-28
7 mm height keV	0	-212	-98	-436	-116	-40	8	-1	-6

Appendix A - BBU tracking code

The tracking code is written as a Mathematica notebook. The bunch is divided longitudinally in a number of slices, or macroparticles, that can be choosen by the user. A gaussian or a uniform charge distribution can also be selected.

The linac is modeled as a series of 32 rf cavities, grouped in 4 cryomodules and separated by drift spaces.

The transverse coordinate x_i of each slice at the exit of the *i-th* cavity is calculated as a function of the displacement x_{i-1} and angle x'_{i-1} at the exit of the preceding cavity:

$$x_i = x_{i-1} + x'_{i-1} L_{drift} + x'_{i-1} L_{cav} + \Delta x'_{i-1} \frac{L_{cav}}{2} \tag{A.1}$$

The additional transverse kick $\Delta x'_i$ represents the cumulative effect of the wakefield induced by the upstream macroparticles. The wakefields are calculated using the analytical formula from [3-4].

The macroparticle angle also changes along the linac:

$$x'_i = x'_{i-1} + \Delta x'_{i-1} - \frac{x_{i-1}}{2L_{cav}} \left(\frac{\Delta\gamma}{\gamma_{i-1}} \right)^2 \tag{A.2}$$

where the effect of the RF focussing is taken into account by the last term in Equation (A.2).

It is also possible to introduce misalignments between cavities and cryomodules and cryomodules tilts. Again, the user can choose amongst different statistical distribution for these errors and determine the most probable values for the emittance increase, performing simulations using many sets of randomly generated alignment errors.

Finally, the user can arbitrarily select the betatron phase advance between each linac pass.

REFERENCES

[1] J. Corlett, *et al.*, *LBNL-48171* (2001).
[2] A. Chao, B. Richter, C.-Y. Yao, *SLAC-PUB-2498* (1980).
[3] A. Mosnier, *TESLA 93-11* (1993).
[4] S. De Santis and A. Zholents, *LBNL-49483* (2002).
[5] *TESLA Technical Design Report* (2001).
[6] ALS Alignment Group, *private communication*.
[7] S. Hartman and J. Rosenzweig, *Phys. Rev. E* 47, 2031 (1993).
[8] "MERLIN, a C++ Class Library for Charged Particle Accelerator Simulations," http://www.desy.de/~njwalker/MerlinII/index.htm
[9] J. Rosenzweig and L. Serafini, "Transverse Particle Motion in Radio-Frequency Linear Accelerators," Phys. Rev. E, Volume 49 Number 2, February 1994
[10] "MAD Version 8,":http://www-project.slac.stanford.edu/lc/local/AccelPhysics/Codes/Mad /MAD8.html

[11] M.D.Woodley, private communication
[12] Handbook of Accelerator Physics and Engineering, A. W. Caho and M. Tigner eds, World Scientific, 1998.
[13] L.I. Schiff, Rev. Sci. Instr. 17, 6 (1946).
[14] J.S. Nodvick and D.S. Saxon, Phys. Rev. 96, 180 (1954).
[15] E.L. Saldin, E.A. Schneidmiller, and M.V. Yurkov, NIM A 398, 373 (1997).
[16] R.Li, C.L. Bohn, J.J. Bisognano, Particle Accelerator Conference, 1644 (1997).